CENTER FOR CONNECTED AND AUTOMATED TRANSPORTATION

Report No. ICT-20-010 **November 2018**

Project Start Date: November 2016

Project End Date: September 2018

Development of a Flexible Pavement Design Framework for Autonomous and Connected Trucks

by
Osman Erman Gungor
Imad L. Al-Qadi
University of Illinois at Urbana–Champaign

DISCLAIMER

Funding for this research was provided by the Center for Connected and Automated Transportation under Grant No. 69A3551747105 of the U.S. Department of Transportation, Office of the Assistant Secretary for Research and Technology (OST-R), University Transportation Centers Program. The contents of this report reflect the views of the authors, who are responsible for the facts and the accuracy of the information presented herein. This document is disseminated under the sponsorship of the Department of Transportation, University Transportation Centers Program, in the interest of information exchange. The U.S. Government assumes no liability for the contents or use thereof.

Suggested APA Format Citation:

Gungor, O. E., Al-Qadi, I. L., & Ouyang, Y. (2018). *Development of a flexible pavement design framework for autonomous and connected trucks* (Report No. ICT-20-010). Illinois Center for Transportation. https://doi.org/10.36501/0197-9191/20-010

Contacts:

Osman Erman Gungor
University of Illinois at Urbana–Champaign
Illinois Center for Transportation
1611 Titan Drive
Rantoul, IL 61866
gungor2@illinois.edu
(217) 300-1488
https://ict.illinois.edu

CCAT
University of Michigan Transportation Research Institute
2901 Baxter Road
Ann Arbor, MI 48152
uumtri-ccat@umich.edu
(734) 763-2498
www.ccat.umtri.umich.edu

TECHNICAL REPORT DOCUMENTATION PAGE

1. Report No.	2. Government Accession No.	3. Recipient's Catalog No.
ICT-20-010	N/A	N/A

4. Title and Subtitle	5. Report Date
Development of a Flexible Pavement Design Framework for Autonomous and Connected Trucks	November 2018
	6. Performing Organization Code N/A

7. Authors	8. Performing Organization Report No.
Osman Erman Gungor and Imad L. Al-Qadi	ICT-20-010 UILU-ENG-2020-2010

9. Performing Organization Name and Address	10. Work Unit No.
Illinois Center for Transportation Department of Civil and Environmental Engineering University of Illinois at Urbana–Champaign 205 North Mathews Avenue, MC-250 Urbana, IL 61801	N/A
	11. Contract or Grant No. Grant No. 69A3551747105

12. Sponsoring Agency Name and Address	13. Type of Report and Period Covered
Center for Connected and Automated Transportation University of Michigan Transportation Research Institute 2901 Baxter Road Ann Arbor, MI 48152	N/A
	14. Sponsoring Agency Code Center for Connected and Automated Transportation

15. Supplementary Notes

Funding Grant No. 69A3551747105 U.S. Department of Transportation, Office of the Assistant Secretary for Research and Technology (OST-R), University Transportation Centers Program
https://doi.org/10.36501/0197-9191/20-010

16. Abstract

Lateral position of loading, which is an important input to pavement design and analysis, is a random phenomenon for human-driven trucks because they do not follow a straight path as they travel. Therefore, in the pavement-design community, this variable has been called "wheel wander" and conventionally considered in an implicit way. However, with the introduction of autonomous and connected trucks (ACTs), this variable is expected to be controllable, using the embedded autopilot and communication technologies. Hence, this variable should be taken as an explicit input to simulate accurately the impact of ACTs on pavement-damage accumulation. This study presents a framework that may improve any pavement-damage accumulation approach to take lateral position of loading as an explicit input. Due to utilization of truncated normal distributions, the effects of lane width and vehicle width on pavement-damage accumulation could be considered in the framework as well. In this paper, this framework was applied on the state-of-the-practice pavement-design approach, Mechanistic–Empirical Pavement Design Guideline (MEPDG). MEPDG's damage-accumulation equations were reinforced with curve-fitting and function-approximation techniques for explicit consideration of the lateral position. A simple numerical example was presented in the paper to demonstrate how accumulated damage varies with respect to the position of loading.

17. Key Words	18. Distribution Statement
Autonomous and Connected Trucks, Flexible-Pavement Design Framework, Pavement Damage, Damage Accumulation, Wander, Lateral Position	No restrictions. This document is available through the National Technical Information Service, Springfield, VA 22161.

19. Security Classif. (of this report)	20. Security Classif. (of this page)	21. No. of Pages	22. Price
Unclassified	Unclassified	35	N/A

ACKNOWLEDGMENT, DISCLAIMER, MANUFACTURERS' NAMES

This project was conducted in cooperation with the Center for Connected and Automated Transportation and the Illinois Center for Transportation. The contents of this report reflect the view of the authors, who are responsible for the facts and the accuracy of the data presented herein. The contents do not necessarily reflect the official views or policies of CCAT or ICT. This report does not constitute a standard, specification, or regulation. Trademark or manufacturers' names appear in this report only because they are considered essential to the object of this document and do not constitute an endorsement of the product by CCAT or ICT.

TABLE OF CONTENTS

LIST OF FIGURES

LIST OF TABLES

CHAPTER 1: INTRODUCTION

The US population and economy exhibited significant growth between 2000 and 2014. According to the US Department of Transportation *Freight Fact* reports, while the population grew by 13% to an estimated 319 million in 2014, gross domestic product increased by 24.9%, reaching $15,773,516 (millions of chained dollars). This expansion in the economy and population caused a concurrent increase in truck-freight transportation, which carried 69.6% (by ton) of the total goods moved in 2013. Moreover, a total of 13,732 million tons of goods valued at $11,444 million were shipped by trucks in 2013, representing 9.21% and 6.16% over the estimates of 2007 by ton and value, respectively (USDOT, 2015).

This growing truck traffic and freight demand has created two major issues for the trucking industry. The first is the shortage of truck drivers. According to the American Trucking Associations, the current driver shortage is around 50,000 and is expected to increase to 900,000 over the next eight years (ATA, 2017). The second issue is the increasing operation cost due to congestion. In 2014, according to the American Trucking Research Institute, congestion caused over $49 billion added operation cost in the United States, which in turn may raise the price of transported goods (Pierce & Murray, 2014). To address these issues, numerous technological developments have been introduced in the trucking industry. One such innovation is implementing connected and autonomous vehicle (CAV) technology on trucks.

The research in CAV technologies historically has been driven by small-sized vehicles such as passenger cars or shuttles. However, in the last few years, there has been significant interest in developing autonomous and connected trucks (ACTs), with the motivation of lowering the freight cost. Almost all big companies that have been pioneers in CAV technologies have subsidiaries or departments for ACT development, such as Otto owned by Uber and Waymo owned by Google.

The introduction of ACTs into freight transportation is expected to bring many advantages. These advantages can be grouped into two categories. The first one is addressing the limitations associated with having human as drivers. For example, currently in the United States, truck drivers are not allowed to work more than 11 hours per day and 60 hours per week. This restriction can be relaxed with even a limited level of automation (e.g., level 4), for which a human presence is required within a truck. Ideally, under the assumption of full automation, the operation time can even be extended to 24 hours, which can significantly improve the efficiency of freight transportation and lower the cost. The second group is possible reduction in the operational cost through truck platooning, which can be defined as a convoy of trucks traveling at a close distance. Reducing congestion and braking/accelerating as well as improving safety, traffic flow, and fuel efficiency are some of the reported and expected benefits of platooning.

Although there are, as previously mentioned, many reported and expected advantages of using ACTs in freight transportation, their adoption is correlated with the condition of the transportation infrastructure. In fact, aging and deteriorating infrastructure is considered by some experts to be one of the main barriers to advancing CAV technologies (RAC, 2017). Given that 20% of roadway miles are in poor or mediocre condition and 9.1% of bridges are structurally deficient or functionally obsolete

(ASCE, 2017), accurate prediction of performance of the infrastructure has become even more important to ensure the presence of a functioning and well-maintained infrastructure network for ACT advancement.

Realistically predicting the behavior of any infrastructure strictly relies on accurate representation of the traffic inputs. As one may expect, currently, the traffic inputs for transportation analysis and design tools are characterized by the nature of human drivers. However, the introduction of ACTs is expected to result in drastic changes in characterization of such inputs, which may require significant modifications to existing infrastructure-design guidelines or development of new guidelines. This report focuses on one such input in pavement design and analysis: lateral position of loading.

Lateral position of loading is one of the most important variables in pavement design and analysis. It is a well-known fact that trucks driven by humans seldom follow a straight path. On the contrary, their lateral position deviates significantly as they travel. This lateral movement of the wheel load is called *wheel wander* in the pavement-design community. The word "wander" implies the inherent randomness of the lateral position of the load for human-driven trucks. The introduction of ACTs is expected to change two main characteristics of the lateral position of loading. The first is that the level of randomness of the lateral position of ACTs will be significantly less. This will create a more channelized traffic load on the pavement and consequently decrease pavement service life, as well as increase maintenance and rehabilitation cost. The second is this variable, lateral position of loading, which is a random variable for human-driven trucks; it will be remotely controllable using autopilot and communication technologies existing in ACTs. This controllability creates opportunities for developing control strategies that laterally shift the trucks to minimize damage (Noorvand et al., 2017).

In the literature, there are flexible-pavement design guidelines that can assess the impact of channelized traffic caused by ACTs. However, to the best of the authors' knowledge, there are no flexible-pavement design guidelines that take the lateral position of a wheel load as an explicit input. Furthermore, the impact of lane and axle width is not currently being considered for damage accumulation within flexible pavement. This study aims to fill this gap by developing a flexible-pavement design framework for ACTs. This framework can explicitly consider lateral position of loading with any level of randomness, which enables it to simulate mixed-traffic conditions where human-driven and ACTs travel over pavement structures. Additionally, lane and axle widths are also incorporated into damage computation by this framework. This framework can incorporate any damage-accumulation approaches (e.g., mechanistic–empirical or mechanistic). This report presents the application of the developed framework on the state-of-the-practice pavement-design guideline Mechanistic-Empirical Pavement Design Guideline (MEPDG) (NCHRP, 2004), which generates a continuous damage profile that presents the accumulated damage through the cross section of pavement instead of reporting a number. This increases the dimensionality of pavement design from 1D (only depth) to 2D.

CHAPTER 2: BACKGROUND

The lateral position of the wheel load is one of the most important variables in flexible-pavement design. As mentioned, it is not a deterministic variable for human-driven trucks, i.e., its value changes in a random fashion. Therefore, this variable is commonly referred as *wheel wander* in the pavement-design community, to imply the inherent randomness. Due to this randomness, all flexible-pavement design guidelines so far have considered this variable implicitly in an averaging sense rather than as an explicit input. This section summarizes the studies that incorporate wheel wander into the flexible-pavement design procedure. However, to apprehend these studies, one should understand the mathematical representation of wheel wander, which is described in this chapter.

WHEEL WANDER DEFINITION

Wheel wander can be interpreted as the uncertainty of the lateral position of wheel loads on a lane. Mathematical representation of wheel wander can be built by defining a variable (d_w) as the distance between the edge of the tire and the road. This distance is not a deterministic value for human-driven trucks, i.e., its value changes in a random fashion. Therefore, it should be modeled using probabilistic approaches when one is designing pavement for human-driven trucks. Figure 1 illustrates the wheel wander on a standard lane layout. This figure assumes that the lane width and axle width are 12 ft and 8.5 ft, respectively.

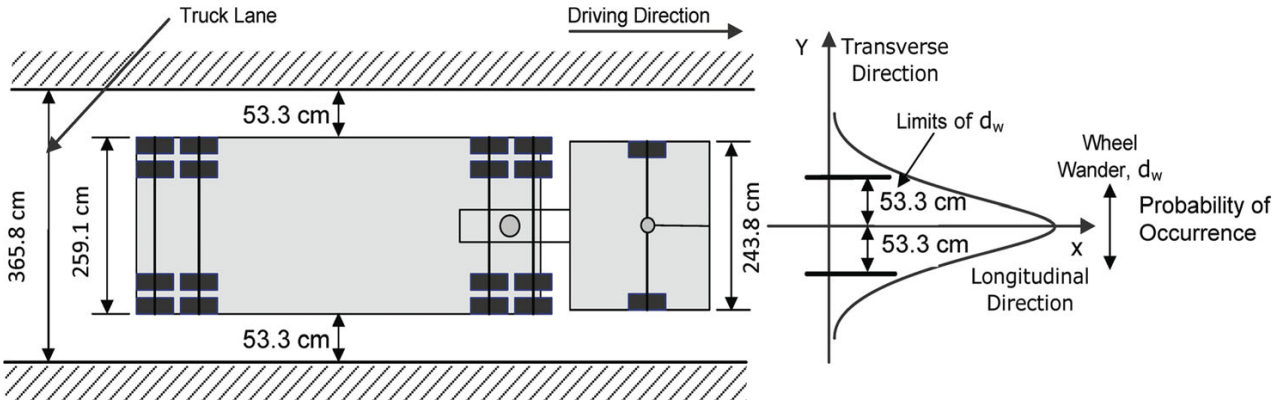

Figure 1. Photo. Demonstration of wheel wander (Siddarthan, 2017).

Probabilistic modeling of wheel wander starts with a conventional assumption that the vehicles are inclined to be centered on the lane with an uncertainty, i.e., their position deviates from its mean location (from the center of the lane) with some probability. Traditionally, this assumption is modelled using a zero-mean normal distribution with a known standard deviation (Figure 2). The value used for standard deviation dictates the level of randomness of wheel wander. NCHRP (2004) recommends 10 in. for the standard deviation.

$$f(d_w) = \frac{1}{\sqrt{2\pi\sigma^2}} e^{-\frac{(d_w-\mu)^2}{2\sigma^2}}$$

Figure 2. Equation. Normal distribution

where μ = mean, and σ = standard deviation.

WHEEL WANDER IN PAVEMENT DESIGN

It is important to incorporate the impact of wheel wander when designing the pavements. Two studies in the literature developed analytical approaches to consider wheel wander in pavement design, based on its definition as given in the previous section.

The first approach was developed by NCHRP (2004) and is illustrated in Figure 4. In the figure, row B shows the damage-accumulation profile whose maximum would be used to compute the pavement service life if there were no wander. Instead, NCHRP computes the average of predicted damages at five discrete locations and uses it as the final damage (Figure 3). The discrete points are selected by moving -1.28155*σ (Figure 2) from the center, five times. Each jump is assumed to represent 20% of the traffic. It is important to note that this approach could only be used for fatigue-crack prediction. In NCHRP, it is stated that "for rutting, the guide software modifies the actual pavement responses for the effects of wander and uses this modified response for the calculation of the incremental permanent deformation within each layer." However, no explanation is provided in the guide as to how the responses get modified.

$$D = 0.2D_1 + 0.2D_2 + 0.2D_3 + 0.2D_4 + 0.2D_5 = \sum_{i=1}^{5} 0.2D_i$$

Figure 3. Equation. Damage index computation under wheel wander

The second approach was developed by Siddharthan et al. (2017). This approach modifies the pavement's structural responses computed by 3D Move software to account for wheel wander. The modification is performed based on Monte Carlo simulation. Later, the modified responses are injected into the empirical functions also used by NCHRP (2004), to predict the damage within the pavement structure. The steps of the approach developed are listed below.

1. Draw a sample from the distribution given in Figure 2.
2. Accept the sample if it is not outside the boundaries (Figure 1).
3. Calculate all critical pavement responses at the accepted sample.
4. Repeat the first three steps 10,000 times.
5. Generate the cumulative distribution function for each critical pavement response.
6. Discretize the cumulative distribution on specific probabilities (e.g., 0%, 20%, 40%, 60%, 80%, 100%).
7. Extract the responses at the selected probabilities and average them.
8. Use the averaged responses in the empirical equations and compute the damage.

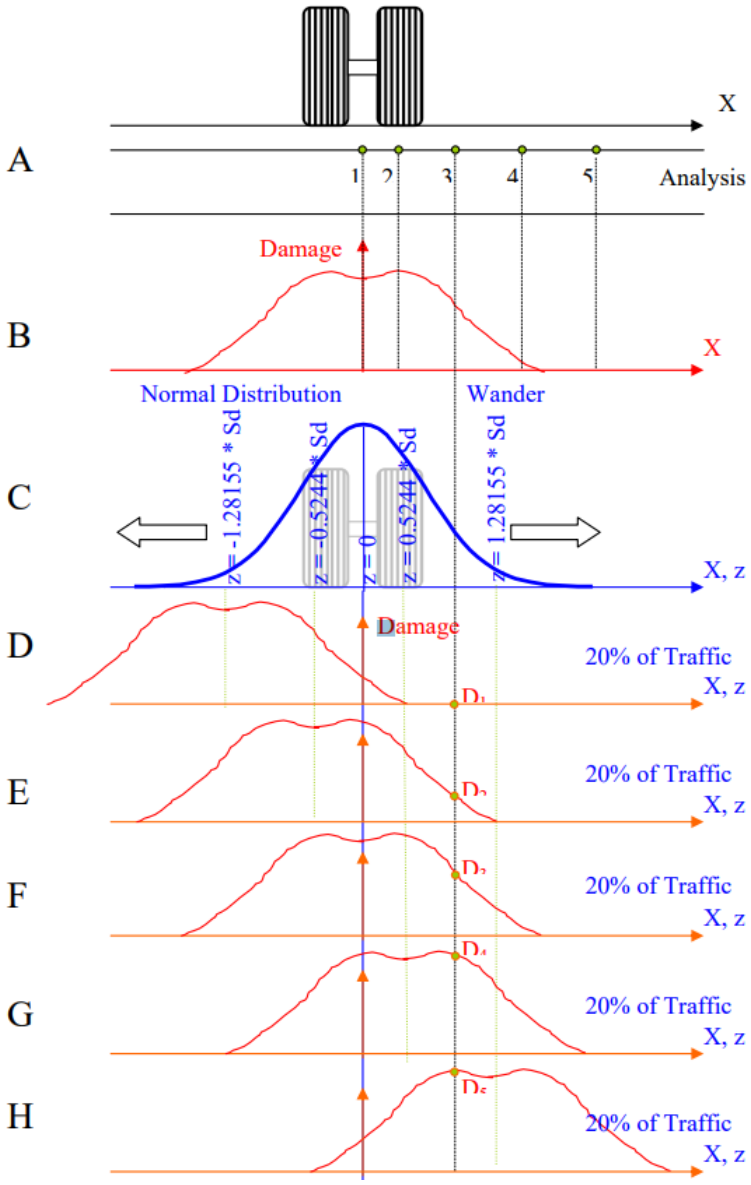

Figure 4. Photo. NCHRP analytical approach for consideration of wheel wander (NCHRP, 2004).

CHAPTER 3: CONCEPT BEHIND THE FRAMEWORK DEVELOPED

The concept behind the proposed approach is illustrated in Figure 5. This figure can be explained in the following way. Let's assume that we have a tire load that is applied right at the center of the wheel path for N number of times (Figure 5-A). Additionally, we have access to the proper tools that compute the damage (i.e., rutting, bottom-up cracking) after this N repetitions. Finally, let's assume that, after computing the damage at discrete locations, we can fit a continuous function (i.e., $g(x)$ in Figure 5-A) that gives the damage profile over the cross section. In this example, what is not certain so far is the lateral position of this tire load. For example, in Figure 5-B, it is assumed that the same load is applied at a different lateral location. Because it is the same load, the magnitude of the damage profile stays the same (i.e., $g(x)$). However, the center of the profile has shifted. We interpret this shift as wheel wander, which is the essence of the framework presented in this report. In other words, we are considering wheel wander as the uncertainty of the center of function $g(x)$. In mathematical terms, we are mapping the domain "x" to "$x - s$" which leads to mapping $g(x)$ to $g(x - s)$. For human-driven trucks, s is a random variable that follows a certain distribution. For autonomous trucks, depending on the assumption, s can be either a random variable with much less uncertainty (e.g., much less standard deviation in the case of a normal distribution) or a deterministic value. If s is a random variable, $g(x - s)$ becomes a random function, which allows us to compute the statistics of the function, such as expectation ($E[g(x - s)]$), which can be interpreted as the resultant accumulated damage profile under wheel wander.

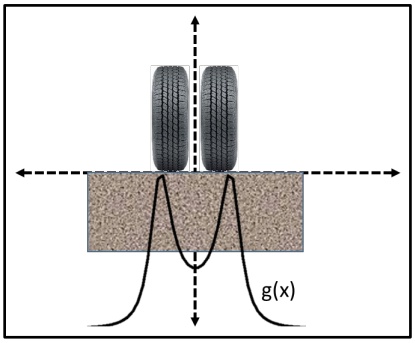

(a) Original loading

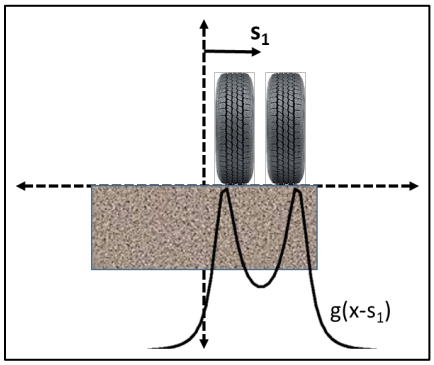

(b) Shifted loading

Figure 5. Photo. Demonstration of the concept behind the framework developed.

CHAPTER 4: IMPLEMENTATION OF THE FRAMEWORK DEVELOPED

It is clear from the previous chapter that the implementation of the framework developed needs a computed damage profile, which can be obtained by any pavement-design approach (e.g., mechanistic, mechanistic–empirical, or even from field tests). In this study, we are applying the framework to the-state-of-the-practice mechanistic–empirical damage-prediction approach (i.e., MEPDG) developed by NCHRP. To fully adopt MEPDG's approach, we utilized a function-approximation technique, namely Chebyshev approximation. Chebyshev approximation was especially important for implementing time-hardening approaches used in MEPDG for rutting simulation. The implementation of the framework developed on MEPDG's approach consists of five steps: extracting responses, curve-fitting, differential damage computation, shifting, and damage accumulation. As explained in the remainder of this report, the order of the steps varies, depending on the distress type (e.g., fatigue cracking or rutting).

EXTRACTING RESPONSES

This step of the framework corresponds to the mechanistic part of MEPDG. In this step, the critical pavement responses are computed under a tire load given material properties and pavement structure. This study used 3D advanced pavement finite-element (FE) models that were developed and continuously improved by Al-Qadi and his coworkers over more than 15 years (Elsefi et al., 2006; Yoo & Al-Qadi, 2007; Wang & Al-Qadi, 2010; Al-Qadi & Wang 2012; Al-Qadi et al., 2015; Gungor et al., 2016a, 2016b; Hernandez & Al-Qadi, 2017; Castillo & Al-Qadi, 2018) as the structural analysis tool for response computation. Using FE models brings the following advantages, as compared to conventional pavement structural analysis approaches (e.g., layered elastic theory) that are summarized in Table 1.

Table 1. Comparison of FE Analysis with Conventional Approaches (Gungor et al., 2017)

Variable Name	FE Analysis	Conventional
Tire loading	3D nonuniform contant stresses	1D uniform tire pressure
Contact area	Realistic irregular tire footprint	Circular contact area
Moving load	Explicitly considered in viscoelastic dynamic analysis	Implicitly considered in dynamic modulus calculations
Tire types	Both WBT and DTA can be simulated	Only DTA can be considered
Friction between layers	Realistic Elastic stick model	Distributed spring model
AC-layer material properties	Viscoelastic characterization using Prony series	Dynamic modulus obtained from master curve
Base layer	Stress-dependent, nonlinear model for base	Linear elastic

Critical Response Locations

The initial step of the damage-prediction framework developed by MEPDG is determining the locations where the responses are extracted. These locations are called *critical locations*. MEPDG provides a two-part procedure for finding critical locations.

The first part determines the critical depths and starts with a sub-layering step that divides each pavement layer into smaller parts. The midpoint of each part (i.e., sub-layer) is considered as a critical depth, which is used for rutting prediction. This study develops the algorithm given in Figure 6 that implements the sub-layering procedure developed by MEPDG. It is important to note that the algorithm is presented here only for the asphalt-concrete layer, the unbound granular layer, and the subgrade layer. Similar algorithms can be developed for other types of layers, such as asphalt-modified base, by following the logic behind the algorithm developed. Other critical depths in addition to the mid-depth of sub-layers are the bottom and top of the AC layers, for fatigue-cracking prediction; and the bottom and 6 in. from the bottom of the last sub-layer, for rutting prediction.

if *Asphalt Layer* **then**
  i = 1; AC_Sublayers[i] = 0
  while $\sum_{i=1} AC\_Sublayers[i] < h_{AC}$ **do**
    if $i = 1$ **then**
      AC_Sublayers[i] = $min\{0.5", h_{AC}\}$
    else if $i = 2$ **then**
      AC_Sublayers[i] = $min\{0.5", h_{AC} - 0.5"\}$
    else if $\sum_{i=1} AC\_Sublayers[i] \geq 1"$ *and* $\sum_{i=1} AC\_Sublayers[i] < 4"$ **then**
      AC_Sublayers[i] = $min\{1", h_{AC} - \sum_{i=1} AC\_Sublayers[i]\}$
    else if $\sum_{i=1} AC\_Sublayers[i] \geq 4"$ *and* $\sum_{i=1} AC\_Sublayers[i] < 8"$ **then**
      AC_Sublayers[i] = $min\{4", h_{AC} - \sum_{i=1} AC\_Sublayers[i]\}$
    else if $\sum_{i=1} AC\_Sublayers[i] \geq 8"$ **then**
      AC_Sublayers[i] = $h_{AC} - \sum_{i=1} AC\_Sublayers[i]$
    i = i + 1
else if *Granular Base Layer* **then**
  i = 1; Base_Sublayers[i] = 0
  while $\sum_{i=1} Base\_Sublayers[i] < h_{Base}$ **do**
    if $i = 1$ **then**
      Base_Sublayers[i] = $min\{2", h_{Base}\}$
    else if $i = 2$ **then**
      Base_Sublayers[i] = $min\{4", h_{Base} - \sum_{i=1} Base\_Sublayers[i]\}$
    i = i + 1
else if *Subgrade Layer* **then**
  i = 1; Subgrade_Sublayers[i] = 0
  while $\sum_{i=1} Subgrade\_Sublayers[i] + h_{AC} + h_{Base} < 8'$ **do**
    Subgrade_Sublayers[i] = $min\{12", 8' - \sum_{i=1} Subgrade\_Sublayers[i] + h_{AC} + h_{Base}\}$
    i = i + 1

Figure 6. Equation. Algorithm 1: Sub-layering algorithm.

The second part of the procedure includes determining critical locations in transverse and traffic directions. In the transverse direction, the critical locations are computed using the set of equations (Figure 7) that are a function of tire spacing ($T_{spacing}$) and radius of the contact area (T_{radius}). In these equations, X_1 corresponds to the center of dual tires. MEPDG uses just these 10 locations, as the tire load is symmetric. However, in FE models, nonuniform contact stresses are used; therefore, we extracted the responses from two sides of the center. Furthermore, in this study, we omitted

critical locations whose values exceed the wheel-path width (i.e., if any of the values of X_is is greater than half of the wheel path, which equals one-quarter of the lane width); and we added the wheel path half-width as a critical location. Thereby, we omitted the critical locations that fall out of the wheel path and capture the response profile through the wheel path. For multi-axle groups (e.g., tandem or tridem), these responses are computed at specific positions in traffic directions, which can be designated as slices in the traffic direction. Each slice is a vector that keeps the computed responses at transverse directions. The lateral movement of tire loading (i.e., wheel wander) does not impact the distribution of responses in the traffic direction. Therefore, to reduce computation complexity, after computing responses at each slice, the maximum slice with the highest response is determined and used for the next steps of the proposed framework. In summary, the outcomes of this step are 1 by 19 vectors that store the extracted responses at each transverse location for each critical depth.

$$
\begin{aligned}
X_1 &= 0.0 \\
X_2 &= \left(\frac{T_{spacing}}{2} - T_{radius}\right) * 0.5 \\
X_3 &= \frac{T_{spacing}}{2} - T_{radius} \\
X_4 &= \frac{T_{spacing}}{2} \\
X_5 &= \frac{T_{spacing}}{2} + T_{radius} \\
X_6 &= \frac{T_{spacing}}{2} + T_{radius} + 4" \\
X_7 &= \frac{T_{spacing}}{2} + T_{radius} + 8" \\
X_8 &= \frac{T_{spacing}}{2} + T_{radius} + 16" \\
X_9 &= \frac{T_{spacing}}{2} + T_{radius} + 24" \\
X_{10} &= \frac{T_{spacing}}{2} + T_{radius} + 32"
\end{aligned}
$$

Figure 7. Equation. Critical responses

DIFFERENTIAL DAMAGE COMPUTATION

The damage-prediction framework developed by MEPDG has two steps. The first step answers the question of how much damage is going to occur when a strain is applied for N times. In other words, the strains are transformed into damage that occurs after a number of load repetitions. This transformation is done by using transfer functions. Herein, we call this step *differential damage computation*. The outcomes of this step are rutting at the mid-depth of each layer and the fatigue-damage index for fatigue-crack prediction.

Whenever an input changes that alters the value of the computed strain (e.g., different modulus due to temperate changes or a different axle load), the differential damage-computation step is repeated.

After each repeat, the outcomes are fed to damage-accumulation equations to predict final damage. These accumulation equations are explained in the section titled "Damage Accumulation." The following sections explain the computation of the parameters in the differential damage computation.

Damage Index

Damage index (DI) is used for predicting fatigue cracking and is computed using the equation in Figure 8.

$$DI = \frac{n}{\vec{N}}$$

Figure 8. Equation. Damage index.

where n = number of load repetitions derived from traffic data; and $\vec{N}$ = vector of computed allowable number of repetitions, using transfer functions at each transverse location.

The current version of the formula (AASHTO, 2015) used for calculating the number of repetitions to failure is given in Figure 9.

$$\vec{N} = k_{f1} C C_H B_{f1} \left(\frac{1}{\vec{\varepsilon_t}}\right)^{k_{f2}\beta_{f2}} \left(\frac{1}{E}\right)^{k_{f3}\beta_{f3}}$$

Figure 9. Equation. Number of repetitions to failure.

where $\vec{\varepsilon_t}$ = vector of extracted tensile strains at the bottom of the AC for each transverse location; E = dynamic modulus of the hot-mix asphalt (HMA) layer (psi); k_{f1}, k_{f2}, k_{f3} = global field-calibration factors: 0.007566, 3.9492, and 1.281, respectively; β_{f1}, β_{f2}, β_{f3} = local calibration factors that are set to 1.0 by default. In addition:

$$C = 10^M$$

$$M = 4.84\left(\frac{V_{be}}{V_a + V_{be}} - 0.69\right)$$

Figure 10. Equation. Some material constants needed for number of repetitions to failure.

where V_{be} = effective asphalt content by volume (%); V_a = percent air voids in the HMA mixture; and C_H = thickness correction term, depending on the type of cracking.

For bottom-up fatigue cracking:

$$C_H = \frac{1}{0.000398 + \frac{0.003602}{1 + e^{11.02 - 3.49 H_{HMA}}}}$$

Figure 11. Equation. Thickness correction term for bottom-up cracking.

For top-down cracking:

$$C_H = \frac{1}{0.01 + \frac{12}{1 + e^{15.676 - 2.8186 H_{HMA}}}}$$

Figure 12. Equation. Thickness correction term for bottom-up cracking.

Asphalt-Concrete (AC) Rutting

The current version of the formula (AASHTO, 2015) used for calculating the rutting within AC is given in Figure 13.

$$\vec{\delta} = h_{sub} \beta_{r1} k_z \overrightarrow{\varepsilon_v} 10^{k_{31}} n^{k_{r2} \beta_{r2}} T^{k_{r3} \beta_{r3}}$$

Figure 13. Equation. Rutting equation for asphalt concrete.

where h_{sub} = thickness of sub-layer (algorithm 1); $\vec{\delta}$ = the vector of predicted rutting at the mid-depth of each sub-layer of the AC layer at each critical transverse location; $\overrightarrow{\varepsilon_v}$ = the vector of vertical compressive strain at the mid-depth of each sub-layer at each critical transverse location; n = repetition number of the load that developed $\varepsilon_{r(AC)}$ at given climatic conditions; T = temperature at the mid-depth of each sub-layer (°F); k_{r1}, k_{r2}, k_{r3} = global field-calibration factors: -3.3512, 0.4791, and 1.5606, respectively; β_{r1}, β_{r2}, β_{r3} = local calibration factors that are set to 1.0 by default. In addition:

$$k_z = (C_1 + C_2 D) 0.328196^D$$

$$C_1 = -0.1039\ h_{AC}^2 + 2.4868 h_{AC} - 17.342$$

$$C_2 = 0.0172 h_{AC}^2 - 1.7331 h_{AC} + 27.428$$

Figure 14. Equation. Some constants needed for rutting calculation.

where D = mid-depth of the sub-layer from the surface (in.) and h_{AC} = total AC thickness.

Rutting in Unbound Layers

The current version of the formula (AASHTO, 2015) used for calculating the rutting within unbound materials is given in Figure 15.

$$\vec{\delta} = h_{sub}\, \beta_{r1} k_{r1} \left(\frac{\varepsilon_0}{\varepsilon_r}\right) e^{-\left(\frac{\rho}{n}\right)^{\beta}} \overrightarrow{\varepsilon_v}$$

Figure 15. Equation. Rutting in unbound layers.

where k_{r1} = global field-calibration factors: 2.03 for granular materials and 1.35 for fine-grained materials; and β_{r1} = local calibration factor, set to 1 by default. In addition:

$$\beta = 10^{0.6119 - 0.017638\, W_c}$$

$$\left(\frac{\varepsilon_0}{\varepsilon_r}\right) = \frac{e^{(\rho^\beta)} a_1 + e^{\left(\frac{\rho}{10^9}\right)^\beta} a_9}{2}$$

$$\rho = 10^9 \left(\frac{C_0}{1 - (10^9)^\beta}\right)^{\frac{1}{\beta}}$$

$$W_c = 51.712 \left[\left(\frac{E}{2555}\right)^{\frac{1}{0.64}}\right]^{-0.3586 * GWT^{0.1192}}$$

$$C_o = ln\left(\frac{a_1}{a_9}\right)$$

Figure 16. Equation. Some material constants required for rutting calculations.

where E = resilient modulus of the sub-layer at mid-depth (psi); GWT = groundwater table depth (ft); a_1 = 0.15; and $a_9 = 20$.

It is important to note that the equation in Figure 15 calculates the plastic strain at the mid-depth of each sub-layer, which goes up to 8-ft depths. For the rest of the subgrade, a special formula is used. This formula is given in Figure 17.

$$\vec{\delta} = \overrightarrow{\varepsilon_0} \left(\frac{1 - e^{-\vec{Q} h_{bedrock}}}{\vec{Q}}\right)$$

Figure 17. Equation. Rutting calculation after 8 ft.

where $\vec{Q} = \frac{1}{6} ln\left(\frac{\overrightarrow{\varepsilon_0}}{\overrightarrow{\varepsilon_6}}\right)$; $\overrightarrow{\varepsilon_0}$, $\overrightarrow{\varepsilon_6}$ = the vectors that store vertical plastic strain at the bottom of the last sub-layer and 6 in. below the the bottom of the last layer (the plastic strains are calculated using the equation in Figure 13 without a thickness term, i.e., without h_{sub}); and $h_{bedrock}$ = depth to bedrock (ft).

CURVE FITTING

This study aims to develop an analytical pavement-design framework that takes the lateral position of loading as input. To develop such an analytical framework, one has to represent the vectors, which store computed DI or rutting at the discrete transverse locations, as a continuous function. In other words, the aforementioned vectors resulting from differential damage computations should be functionalized. This is done by the curve-fitting step of the framework.

The target variable for curve-fitting differs, depending on the type of damage parameter. For fatigue cracking, the curve is fitted to the final computed damage parameter, i.e., the vector of DI ($\overrightarrow{DI}$ in

Figure 8). By contrast, for rutting computation, the curve is fitted directly to the response vector (i.e., $\overleftarrow{\varepsilon_v}$). It should be noted that the motivation behind using different target variables is reducing the complexities in computations. For example, if we fit a curve to the tensile strain vector for the allowable number of computations, it would be computationally challenging to calculate the $k_{f2}\beta_{f2}$ power of this fitted curve (Figures 11 and 12). In the end, fitting the curve to response or damage does not make any difference in terms of results, as only one variable (i.e., response) changes with respect to the location.

Various curve-fitting techniques are suggested in the literature, e.g., polynomial regression, ridge regression, artificial neural networks (ANNs), and so on. Although some of these techniques are more accurate than others, they have high computational cost (e.g., ANNs or other machine-learning algorithms). Given that the steps of this framework are to be repeated for each different loading and climate condition, computationally costly methods were avoided. In this study, the least-squares regression using the basis-expansion method was utilized (Figure 18). In this equation, there are two unknowns: the basis function ($\phi(x)$) and the regression coefficient (α_i), which are explained in the following section. It should be noted that hereinafter, we denote "x" as a continuous axis that represents the cross section of a wheel path.

$$f(x) = \sum_{i=0}^{n} \alpha_i \phi(x)^i$$

Figure 18. Equation. Curve fitting equation.

where $f(x)$ = fitted curve or function.

Input Transformation Using a Basis Function

It should be observed that if $\phi(x)$ is set to x, Figure 18 becomes identical to the least-squares polynomial regression. However, polynomial regression did not produce a good fit, especially if the load is applied by a dual-tire assembly (DTA) and the response is near the surface. For example, Figure 23-A represents the extracted vertical compressive strains within the AC layer under a DTA loading. This type of loading manifests itself into as an M-shaped data distribution, where the responses are maximized under two tires and exponentially decay away from the tires. The issue with this type of data distribution is that it cannot be represented by a polynomial regression in their original space. To address this issue, we transform the data into a new space where data become smoother, so that we can fit a polynomial accurately. The transformation is conducted in two steps.

The first step is linear mapping of x into a new space that is bounded by -1 and 1. Figure 19 gives the formula for the mapping process. This step can be interpreted as normalization of data.

$$x' = \frac{x}{w_h}$$

Figure 19. Equation. Normalization.

where x' = linearly transformed x, and w_h = wheel-path width that equals 0.25 times the lane width.

The second step is the nonlinear transformation of x' using an exponential function (Figure 20) as the basis function. The transformed data is given in Figure 23-B. In this figure, we define a new variable z that is the transformed version of x. It should be observed from this figure that the data are much smoother, as compared to the original space.

$$z = \phi(x) = exp\left(-\frac{x'^2}{\gamma^2}\right)$$

Figure 20. Equation. Non-linear transformation.

where z = transformed variable, and γ^2 = smoothing constant. The recommended values are 0.1 for fitting the curve to rutting within AC, 0.5 for fitting the curve to rutting in the base/subgrade and fitting the curve to the damage index.

Least-Squares Regression

The equation in Figure 21 gives a modified version of Figure 18, where the constructed variable z is substituted for $\phi(x)$. As can be seen, this equation is nothing but polynomial regression in the transformed space z, whose weight coefficients (α_i) can easily be computed using the least-squares technique. The fitted polynomial in the transformed and original spaces is illustrated in Figures 23-C and 23-D, respectively.

$$f(z) = \sum_{i=0}^{n} \alpha_i z^i = \alpha_0 + \alpha_1 z + \alpha_2 z^2 \dots \alpha_n z^n$$

Figure 21. Equation. Least square regression.

where n = degree of the polynomial. The recommended values are 6 for fitting the curve to rutting within AC and base, 2 for fitting the curve to rutting within the subgrade and for fitting the curve to the damage index.

As can be seen from Figure 23, the response vector $\overrightarrow{\varepsilon_v}$ (Figure 23-A) is represented by a continuous function (Figure 23-D). After fitting the curve to the response, one can easily compute the rutting profile by multiplying this function with the constants given in the rutting equations, which also makes computed rutting a continuous function. The equations below represent the continuous forms of vectors defined in the differential damage-computation stage. As can be seen from the equations and as previously mentioned, the curve is fitted to the damage index (i.e., DI) for the case of fatigue-crack prediction rather than to the responses by following the same curve-fitting steps.

$$\text{For the damage index: } \overrightarrow{DI} \rightarrow DI(x, \vec{C})$$
$$\text{For rutting: } \vec{\delta} \rightarrow \delta(\varepsilon_v(x), \vec{C}$$

Figure 22. Equation. From discrete space to continuous space.

where $DI(x, \vec{C})$ = function fitted to $\overrightarrow{DI}$; $\delta(\varepsilon_v(x), \vec{C})$ = functionalized version of $\vec{\delta}$ due to fitting the curve to $\overrightarrow{\varepsilon_v}$. Hereinafter, we denote this function as $\delta(x, \vec{C})$ for brevity; $\vec{C}$ = vector that stores the required constants, such as calibration factors and temperature.

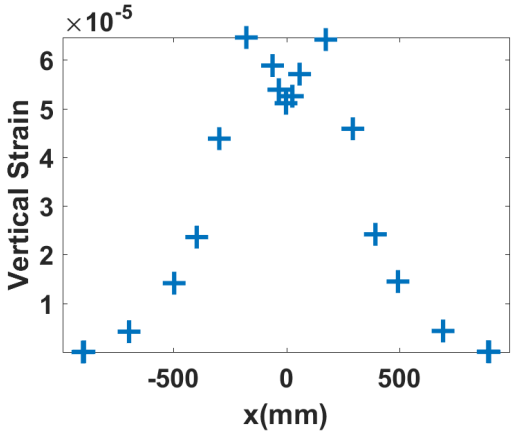

(a) Extracted vertical strain at critical locations

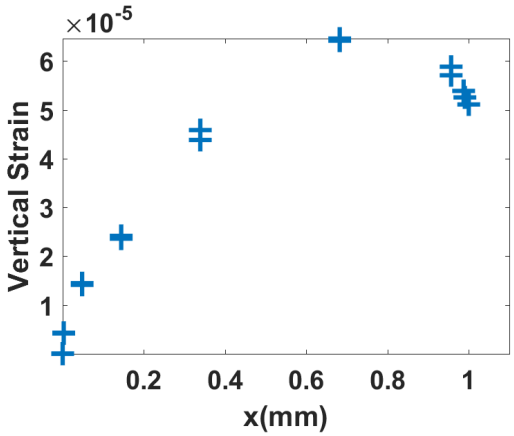

(b) Transformed data

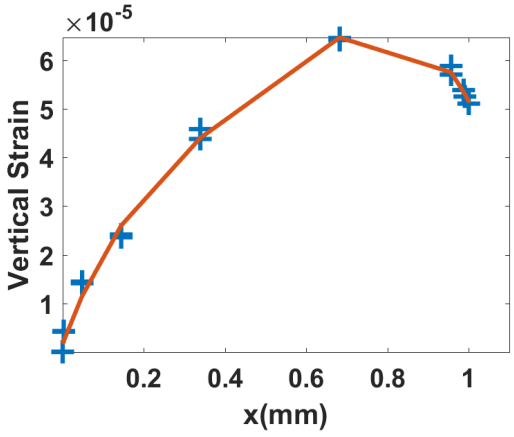

(c) Fitted polynomial in transformed space

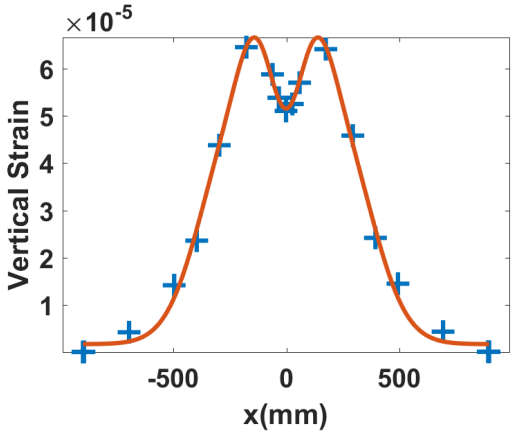

(d) Fitted polynomial in original space

Figure 23. Graph. The steps of curve-fitting.

SHIFTING

As described in Chapter 3, we interpret wheel wander as the shift of the function that represents a damage parameter. Also, as previously mentioned, the framework developed can consider two types of shifting: (1) deterministic, which can be interpreted as ACTs with advanced technology so that they do not exihibit any random lateral movement as they travel; and (2) probabilistic, which can incorporate randomness on the lateral position of the vehicles (i.e., wheel wander) at any level. Furthermore, we also defined the mathematical formulation for shifting, which is basically mapping x to $x - s - t$ where s stands for a random variable for wheel wander, and t for deterministic shifting. It should be noted that, hereinafter, we use the terms *wheel wander* and *probabilistic shifting* interchangeably.

The first step of the shifting is writing the equation in Figure 21 in terms of x by tracing back the transformation described in Figures 19 and 20, which results in the equation in Figure 24.

$$f(x) = \sum_{i=0}^{n} \alpha_i \left(e^{-\left(\frac{x}{w_h \gamma}\right)^2} \right)^i = \sum_{i=0}^{n} \alpha_i e^{-i\left(\frac{x}{w_h \gamma}\right)^2}$$

Figure 24. Equation. Fitted equation.

Afterwards, the shifting (i.e., mapping) can be applied as follows:

$$f(x,t,s) = \sum_{i=0}^{n} \alpha_i e^{-i\left(\frac{x-t-s}{w_h \gamma}\right)^2}$$

Figure 25. Equation. Applying deterministic and probabilistic shifting.

In Figure 25, $f(x, s, t)$ has become a random function due to the variable s. To compute the resultant damage profile, the expectation of this function (i.e.,$E[f(x, s, t)]$) should be calculated. For only deterministic shifting (where s equals zero and t equals some real number), the calculation of expectation is straightforward, and it is done by substituting the value of t into the equation in Figure 25.

For example, the blue line in Figure 29-A demonstrates the rutting profile that is computed by multiplying the fitted response curve (Figure 23-A) by other constants (Table 2) according to Figure 13. If we want to apply deterministic shifting (e.g., t = 300 mm) to this rutting profile (Figure 23-A), we insert 300 mm into Figure 25, which results in a shifted rutting profile demonstrated by the red line in Figure 29-A. It should be observed from this figure that because there is no randomness (i.e., wheel wander), the magnitude of the damage did not change with the shifting, only the locations changed. This kind of shifting should be interpreted in the following way. Instead of applying N road repetitions at the center of the load that gave the profile in the blue line, the loads were applied 300 mm away from the center of the wheel path that produced the red line.

Computation of the damage profile under probabilistic shifting, however, is not as straightforward because it involves integration of the function over the random variable. Before explaining how to compute the expectation, we introduce the random variable.

Truncated Normal Distribution

Traditionally, the normal distribution (Figure 2) is used for modeling wheel wander. What normality essentially indicates is that the distribution of data points looks like a bell-shaped curve, in which most probable data occur around the mean, while other data points occur with an exponentially decaying probability with respect to their distance from the mean. Because most of the data in engineering problems exhibit this kind of behavior, a normal distribution is one of the most commonly used distributions for simulating probabilistic events.

Although the wheel-wander data may pass the normality test, the use of a normal distribution may not be appropriate for modeling wheel wander because of its infinite support (i.e., a normally distributed variable can take values from ∞ to $-\infty$). In other words, the lateral position of the truck can not change between ∞ and $-\infty$. Therefore in this study, for the first time to the best of the authors' knowledge, we are proposing to use a truncated normal distribution for wheel-wander modeling.

The formula of a truncated normal distribution is given in Figure 26, which actually makes the support of a normally distributed random variable finite by bounding it at one or both ends. As can be seen from Figure 26, using a truncated normal distribution allows explicit consideration of lane width, axle width, and tire types in simulating damage accumulation under wheel wander.

$$g_s(s, \mu, \sigma, L, U) = \frac{\phi\left(\frac{s-\mu}{\sigma}\right)}{\sigma\left(\Phi\left(\frac{U-\mu}{\sigma}\right) - \Phi\left(\frac{L-\mu}{\sigma}\right)\right)}$$

Figure 26. Equation. Truncated normal distribution.

where s = a normally distributed random variable; μ = mean of s; σ = standard deviation of s; $\phi(\cdot)$, $\Phi(\cdot)$ = probability density and cumulative distribution function of a standard normal distribution, respectively; L = lower bound, which equals $-\frac{l_w - A_w}{2} - I_{t<0}t$; U = upper bound, which equals $\frac{l_w - A_w}{2} - I_{t>0}t$; l_W = lane width; A_w = axle width that is a function of tire type; and $I_B(t)$ = identity function that equals 1 if condition B is satisfied, 0 otherwise.

It should be noted that a couple of experimental studies in the literature question/disprove the normality assumption of the wheel-wander distribution (Islam et al., 2014; Luo & Wang, 2013). These studies suggest different types of distributions. Although the results presented here are based on normal distributions, any distribution can be truncated and easily incorporated into the framework developed.

Expectation Computation

To get the damage profile, one should compute the expectation of Figure 25 as follows.

$$E[f(x,t,s)]] = \overline{f(x,t)} = \int_L^U \frac{\phi\left(\frac{s-\mu}{\sigma}\right)}{\sigma\left(\Phi\left(\frac{U-\mu}{\sigma}\right) - \Phi\left(\frac{L-\mu}{\sigma}\right)\right)} \left(\sum_{i=0}^{n} \alpha_i e^{-i\left(\frac{x-t-s}{w_h \gamma}\right)^2}\right) ds$$

$$= \sum_{i=0}^{n} \alpha_i \int_L^U \frac{\phi\left(\frac{s-\mu}{\sigma}\right)}{\sigma\left(\Phi\left(\frac{U-\mu}{\sigma}\right) - \Phi\left(\frac{L-\mu}{\sigma}\right)\right)} e^{-i\left(\frac{x-t-s}{w_h \gamma}\right)^2} ds$$

$$= K \sum_{i=0}^{n} e^{-\frac{i(\mu+t-x)^2}{2i\sigma^2+\gamma^2 w_h^2}} [erf(K_U) - erf(K_L)] \frac{\gamma \sigma w_h}{2\sqrt{2i\sigma^2 + \gamma^2 w_h^2}}$$

Figure 27. Equation. Expected value computation.

with

$$K = \frac{1}{\sigma\left(\Phi\left(\frac{U-\mu}{\sigma}\right) - \Phi\left(\frac{L-\mu}{\sigma}\right)\right)}$$

$$K_U = \frac{\gamma^2(U-\mu)w_h^2 + 2i\sigma^2(U+t-x)}{\gamma \sigma w_h \sqrt{4i\sigma^2 + 2\gamma^2 w_h^2}}$$

$$K_L = \frac{\gamma^2(L-\mu)w_h^2 + 2i\sigma^2(L+t-x)}{\gamma \sigma w_h \sqrt{4i\sigma^2 + 2\gamma^2 w_h^2}}$$

Figure 28. Equation. Some constants needed for expected value.

where $\text{erf}(x) = \frac{2}{\sqrt{\pi}} \int_0^x e^{-t^2} dt$ = error function, which can be computed using readily available functions.

Figure 29-B shows the rutting profile ($\overline{f(x,t)}$) computed, considering wheel wander for σ equals 250 mm and μ equals zero (values recommended by MEPDG). It should be noted that both magnitude and location of maximum damage have changed under wheel wander. While the maximum damage is observed right under the tires for the deterministic case (blue line), it moves to the center of the tires for the probabilistic case (red line). A field study (Wu & Harvey, 2008) that compared the rutting profiles with and without channelized load application validates this observation.

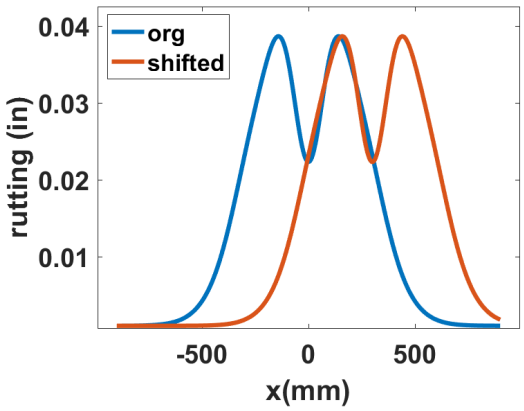

(a) Damage profile shifted by 300 mm

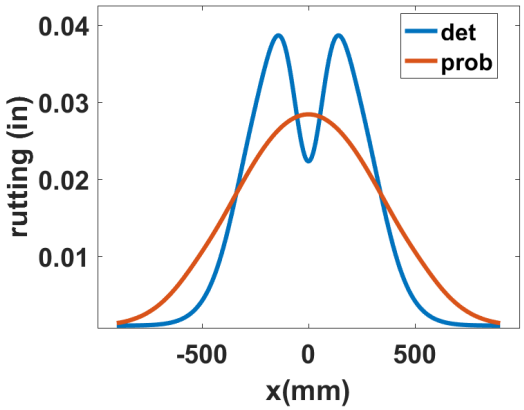

(b) Transformed data

Figure 29. Graph. Application of shifting.

DAMAGE ACCUMULATION

In the section titled "Differential Damage Computation," we presented various transfer functions that input a critical strain, along with the number of repetitions and output rutting or damage index. Any change in loading and/or climatic conditions also changes the value of critical strains and, hence,

requires recomputation of rutting and damage index. This results in a series of computed rutting and damage indices after each load application (i.e., step). After each step, computed damages are accumulated, using damage-accumulation equations. These equations differ for rutting and fatigue cracking, as explained in the following sections.

Rutting Accumulation

MEPDG uses a nonlinear strain-hardening approach to simulate the rutting accumulation after each step. This approach starts with computation of the equivalent repetition (n_{eq}), which is defined as the number of repetitions that would cause the previously accumulated rutting, using the current computed vertical strain. Figure 30 formulates this statement with n_{eq} the only unknown variable.

$$\overline{\delta_{acc}(x)} = \delta(T_i, \overline{\varepsilon_{vi}(x)}, n_{eq}(x), \vec{C})$$

Figure 30. Equation. Rutting accumulation after applying shifting.

where $\overline{\delta_{acc}(x)}$ = accumulated rutting profile until the i^{th} step at each transverse location, considering wheel wander; $\overline{\varepsilon_{vi}(x)}$ = fitted function to extracted compressive strains at the critical locations at the i^{th} step after applying shifting; $n_{eq}(x)$ = profile of the equivalent number of repetitions, which amounts to the solution of Figure 25; and $\delta(T_i, \overline{\varepsilon_{vi}(x)}, n_{eq}(x))$ = predicted rutting profile at each transverse location, which can be computed using empirical functions given in Figures 12, 13, and 14, depending on the material type under the loading and climatic conditions (e.g., T_i) at the i^{th} step.

After solving the equation in Figure 30, $n_{eq}(x)$ is added to the number of repetitions of the current strain. Finally, the total number of repetitions, along with the current strain, is plugged into rutting empirical functions to compute the accumulated rutting (Figure 31).

$$\overline{\delta_i(x)} = \delta(T_i, \overline{\varepsilon_{vi}(x)}, n_{eq}(x) + n_i, \vec{C})$$

Figure 31. Equation. Accumulated rutting at step i.

where $\overline{\delta_i(x)}$ = accumulated rutting profile at the i^{th} step; and n_i = number of repetitions at the i^{th} step.

Finally, total rutting is computed by summing the accumulated rutting at each sub-layer (Figure 32).

$$RD_i(x) = \sum_{j=1}^{M} \overline{\delta_{ji}(x)}$$

Figure 32. Equation. Total rutting, summation of rutting from each layer.

where RD_i = total accumulated rutting profile at the i^{th} step; and M = number of sub-layer.

Fatigue Cracking

Damage accumulation for fatigue cracking is simulated using Miner's Law, given in Figure 33.

$$D_i(x) = \sum_{k=1}^{i} DI_k(x)$$

Figure 33. Equation. Accumulated damage index at step i.

where $D_i(x)$ = accumulated fatigue-damage profile at the i^{th} step.

Afterwards, using the transfer functions given in Figures 34 and 35, the resultant bottom-up and top-down fatigue cracking is computed.

$$FC_i^{bottom}(x) = \left(\frac{1}{60}\right)\left(\frac{C_4}{1 + e^{C_1C_2^* + C_2C_2^* log(D(x)*100)}}\right)$$

Figure 34. Equation. Bottom-up cracking.

where $FC_i^{bottom}(x)$ = percent of alligator-cracking profile that initiates at the bottom of the HMA layers at the i^{th} step; C_1, C_2, C_4 = calibration factors that equal 1, 1, 6, respectively; C_1^* = -2C_2^*; C_2^* = $-2.40874 - 39.748(1 + h_{ac})^{-2.856}$. In addition:

$$FC_i^{top}(x) = 10.56\left(\frac{C_4}{1 + e^{C_1 - C_2 log(D(x)*100)}}\right)$$

Figure 35. Equation. Top-down cracking.

where $FC_i^{top}(x)$ = length of longitudinal cracking profile that initiates at the top of the HMA layer (ft/mi) at the i^{th} step; and C_1, C_2, C_4 = calibration factors that equal 7, 3.5, 1, respectively.

International Roughness Index (IRI)

After computing the distress profile, the international roughness profile ($IRI(x)$) can be computed as follows.

$$IRI(x) = IRI_0 + C_1(RD) + C_2FC_{total} + C_3TC + C_4SF$$

Figure 36. Equation. IRI.

where IRI_0 = initial IRI after construction in./mi; RD = accumulated rutting depth from all layers (in.); FC_{total} = total amount of fatigue cracking, summation of bottom-up and top-down cracking; TC = thermal cracking. It should be noted that because thermal cracking is not load-related distress, it is not studied in this paper. The amount of accumulated thermal cracking can be computed by running commercial AASHTOWare software and integrated into the framework; C_1, C_2, C_3, C_4 = calibration factors, which equal 40, 0.4, 0.008, and 0.015, respectively; and SF = site factor given by

$$SF = Age^{1.5}\left[ln\left((Precip + 1) + (FI + 1)_{p_{02}}\right)\right] + \left[ln\left((Precip + 1) + (PI + 1)_{p_{200}}\right)\right]$$

Figure 37. Equation. Site factor.

where Age = pavement age in years; PI = percent plasticity index of soil; FI = average annual freezing index (°F); $Precip$ = average annual precipitation of rainfall (in.); p_{02} = percent passing the 0.02 mm sieve; and p_{200} = percent passing the 0.075 mm sieve.

CHEBYSHEV APPROXIMATION TO ACCUMULATED DAMAGE

Accumulated-damage equations become too complex to store and compute after a couple of accumulation steps due to the use of continuous functions. This creates the need to simplify the equations using function approximation. In the following paragraph, we demonstrate this issue by giving an example of rutting accumulation on one of the sub-layers within the AC.

In this example, we simulate three steps. We assume that the computed vertical strains after applying shifting and their corresponding repetitions are $\{\overline{\varepsilon_{v1}(x)}, n_1\}$, $\{\overline{\varepsilon_{v2}(x)}, n_2\}$, $\{\overline{\varepsilon_{v3}(x)}, n_3\}$. AC-rutting accumulation starts with computing rutting using the empirical functions given in Figure 13 for $\{\overline{\varepsilon_{v1}(x)}, n_1\}$, which is denoted as $\overline{\delta_1(x)}$ in Figure 38. This amounts to the total rutting profile at the first step. Later, the equivalent repetition $n_{eq}(x)$ for the second step is calculated by solving Figure 25. The result is given in Figure 39. Afterwards, the total rutting profile at the second step is calculated by plugging the total repetition $(n_{eq}(x) + n_2)$ into Figure 30, as given in Figure 40. The rutting profile for the third step can be computed by following the exact steps given in Figures 41 and 42.

$$\overline{\delta_1(x)} = h_{sub}\beta_{r1}k_z\overline{\varepsilon_{v1}(x)}10^{k_{31}}n_1^{k_{r2}\beta_{r2}}T_1^{k_{r3}\beta_{r3}}$$

Figure 38. Equation. Accumulated rutting at step 1.

$$n_{eq}(x) = \left(\frac{\overline{\varepsilon_{v1}(x)}n_1^{k_{r2}\beta_{r2}}T_1^{k_{r3}}}{\overline{\varepsilon_{v2}(x)}T_2^{k_{r3}}}\right)^{\frac{1}{k_{r2}\beta_{r2}}}$$

Figure 39. Equation. Number equivalent repetition at step 2.

$$\overline{\delta_2(x)} = h_{sub}\beta_{r1}k_z\overline{\varepsilon_{v2}(x)}10^{k_{31}}\left(n_2 + \left(\frac{\overline{\varepsilon_{v2}(x)}n_1^{k_{r2}\beta_{r2}}T_1^{k_{r3}}}{\overline{\varepsilon_{v2}(x)}T_2^{k_{r3}}}\right)^{\frac{1}{k_{r2}\beta_{r2}}}\right)^{k_{r2}\beta_{r2}} T_2^{k_{r3}\beta_{r3}}$$

Figure 40. Equation. Accumulated rutting at step 2.

$$n_{eq}(x) = \left(\frac{\left(n_2 + \left(\frac{\overline{\varepsilon_{v1}(x)} n_1^{k_{r2}\beta_{r2}} T_1^{k_{r3}}}{\overline{\varepsilon_{v2}(x)} T_2^{k_{r3}}} \right)^{\frac{1}{k_{r2}\beta_{r2}}} \right)^{k_{r2}\beta_{r2}} T_2^{k_{r3}\beta_{r3}} \overline{\varepsilon_{v2}(x)}}{\overline{\varepsilon_{v3}(x)} T_3^{k_{r3}\beta_{r3}}} \right)^{\frac{1}{k_{r2}\beta_{r2}}}$$

Figure 41. Equation. Number equivalent repetition at step 3.

$$\overline{\delta_3(x)} = h_{sub}\beta_{r1}k_z\overline{\varepsilon_{v3}(x)}10^{k_{31}}$$

$$n_3 \left(\frac{\left(n_2 + \left(\frac{\overline{\varepsilon_{v1}(x)} n_1^{k_{r2}\beta_{r2}} T_1^{k_{r3}}}{\overline{\varepsilon_{v2}(x)} T_2^{k_{r3}}} \right)^{\frac{1}{k_{r2}\beta_{r2}}} \right)^{k_{r2}\beta_{r2}} T_2^{k_{r3}\beta_{r3}} \overline{\varepsilon_{v2}(x)}}{\overline{\varepsilon_{v3}(x)} T_3^{k_{r3}\beta_{r3}}} \right)^{\frac{1}{k_{r2}\beta_{r2}}} k_{r2}\beta_{r2} T_3^{k_{r3}\beta_{r3}}$$

Figure 42. Equation. Accumulated rutting at step 3.

As can be seen, the accumulation equations become too complex to compute even after three steps (the accumulation steps can go into the hundreds). Furthermore, they involve taking the decimal power (e.g., $k_{r2}\beta_{r2}$) of continuous functions (i.e., the shifted version of fitted curves, as given in Figure 25), which is computationally challenging. Therefore, to make the damage-accumulation equations feasible to compute and process, we use Chebysev function approximation, which transforms these complex equations into linear combinations of Chebyshev polynomials in an accurate and efficient way.

Chebysev Approximation

The general formula for Chebyshev polynomials is given in Figure 43.

$$R_p(y) = cos(pcos^{-1}(y)) = y^p \sum_{k=0}^{*\frac{p}{2}} p_{2k}(1 - y^{-2})^k$$

Figure 43. Equation. Chebyshev polynomials.

where R_p = p^{th} degree Chebyshev polynomial and y = real numbers between -1 and 1. Using Chebyshev polynomials, any bounded continuous functions can be approximated, as given in Figure 44.

$$g(y) \approx \sum_{k=0}^{p} h_k R_k(y)$$

Figure 44. Equation. Chebyshev approximation.

where $g(y)$ = the function to be approximated, and h_k = Chebyshev coefficients calculated using Figure 45.

$$\text{For k} = 0\text{: h}_0 = \frac{1}{p+1}\sum_{j=0}^{p} g(b_j)$$

$$\text{For k} > 0\text{: h}_k = \frac{2}{p+1}\sum_{j=0}^{p} g(b_j) R_k(b_j)$$

Figure 45. Equation. Chebyshev coefficients.

where b_j = Chebyshev nodes computed by $cos\left(j\frac{2j+1}{2p+2}\pi\right)$ where $j \geq 0$.

Using Chebyshev function approximation, one can transform the complicated damage-accumulation formula (e.g., Figure 42) into a much simpler form. Thereby, instead of the complex equations, the computed Chebyshev coefficients (i.e., h_k) are enough to store, representing the accumulated damage profile at any given step. In this report, we present separate algorithms that simulate the accumulation of rutting and damage index.

Chebyshev Approximation for Rutting Accumulation

The algorithm to simulate rutting accumulation for any sub-layer within AC, by using Chebysev approximation, is given in Figure 46. Although the equations look complex, their computation is easy because every function is evaluated point-wise at Chebyshev nodes. For this algorithm, we introduce a few more notations, which are explained in the following.

- $\widetilde{\delta(x)^i}$ is the approximated rutting profile using Chebyshev approximation at the i^{th} step.
- Similarly, we denote the variables whose values can change at each step *i* with a subscript *i* (e.g., temperature (T_i), or vertical strain curve ($\overline{\varepsilon_{vi}}$)).

Chebyshev Approximation for Fatigue-Damage Accumulation

Chebyshev approximation for fatigue accumulation is much more straightforward, as compared to rutting, due to linear damage accumulation (i.e., Miner's Law), which allows us to fit the curve of the damage index (Figure 8) rather than the response. The algorithm for fatigue accumulation is given in Figure 47. We introduce one more notation for this algorithm, which is explained in the following.

- $DI(b_j)$ is the value of the fitted curve to damage index (see the section titled "Curve-Fitting").

for $i = 1$ *to* M *(Total Number of Steps)* **do**

if $i = 1$ **then**

Computing Chebyshev Coefficients

For any sub-layer within AC:

$$H_k = h_{sub}\beta_{r1}k_z 10^{k_{31}} n_1^{k_{r2}\beta_{r2}} T_1^{k_{r3}\beta_{r3}} \frac{2}{p+1} \sum_{j=0}^{p} \overline{\varepsilon_{v1}}(b_j) R_k(b_j) \text{ for } k \geq 0$$

For any sub-layer within unbound materials until 8ft:

$$H_k = h_{sub}\beta_{r1}k_{r1} \left(\frac{\varepsilon_0}{\varepsilon_r}\right)_1 e^{-\left(\frac{\rho_1}{n_1}\right)^{\beta_1}} \frac{2}{p+1} \sum_{j=0}^{p} \overline{\varepsilon_{v1}}(b_j) R_k(b_j) \text{ for } k \geq 0$$

After 8 ft:

$$H_k = h_{sub}\beta_{r1}k_{r1} \left(\frac{\varepsilon_0}{\varepsilon_r}\right)_1 e^{-\left(\frac{\rho_1}{n_1}\right)^{\beta_1}} \frac{2}{p+1} \sum_{j=0}^{p} \overline{\varepsilon_{v1}}(b_j) \left(\frac{1-e^{-Q_1(b_j)h_{bedrock}}}{Q_1(b_j)}\right) R_k(b_j) \text{ for } k \geq 0$$

else if $i>1$ **then**

n_{eq} calculations using Equation 20

For any sub-layer within AC

$$r(b_j) = \frac{\overline{\delta(b_j)}^{i-1}}{h_{sub}\beta_{r1}k_z\overline{\varepsilon_{v1}(b_j)}10^{k_{31}}T_i^{k_{r3}\beta_{r3}}} ; n_{eq}(b_j) = r(b_j)^{\frac{1}{k_{r2}\beta_{r2}}}$$

For any sub-layer within unbound materials

$$r(b_j) = \frac{\overline{\delta(b_j)}^{i-1}}{\overline{\varepsilon_{vi}(b_j)}h_{sub}\beta_{r1}k_{r1}\left(\frac{\varepsilon_0}{\varepsilon_r}\right)_i} ; n_{eq}(b_j) = \rho_i \left[-ln\left(r(b_j)\right)\right]^{\frac{-1}{\beta_i}} \text{ (until 8ft)}$$

$$r(b_j) = \frac{\overline{\delta(b_j)}^{i-1} Q_i(b_j)}{\overline{\varepsilon_{v0i}(b_j)}\left(1-e^{-Q_i(b_j)h_{bedrock}}\right)\beta_{r1}k_{r1}\left(\frac{\varepsilon_0}{\varepsilon_r}\right)_i} ; n_{eq}(b_j) = \rho_i \left[-ln\left(r(b_j)\right)\right]^{\frac{-1}{\beta_i}} \text{ (after 8ft)}$$

Computing Chebyshev Coefficients

For any sub-layer within AC:

$$H_k = \frac{2}{p+1} \sum_{j=0}^{p} \left[h_{sub}\beta_{r1}k_z 10^{k_{31}} T_i^{k_{r3}\beta_{r3}} \overline{\varepsilon_{vi}}(b_j)(n_i + n_{eq}(b_j))^{k_{r2}\beta_{r2}} I_{r(b_j)\leq 1} + \widetilde{\delta(x)}^{i-1} I_{r(b_j)>1} \right] R_k(b_j)$$

For any sub-layer within unbound materials until 8ft:

$$H_k = \frac{2}{p+1} \sum_{j=0}^{p} \left[h_{sub}\beta_{r1}k_{r1} \left(\frac{\varepsilon_0}{\varepsilon_r}\right)_i e^{-\left(\frac{\rho_i}{(n_i+n_{eq}(b_j))}\right)^{\beta_i}} \overline{\varepsilon_{v1}}(b_j) I_{r(b_j)\leq 1} + \widetilde{\delta(x)}^{i-1} I_{r(b_j)>1} \right] R_k(b_j)$$

After 8 ft:

$$H_k = \frac{2}{p+1} \sum_{j=0}^{p} \left[h_{sub}\beta_{r1}k_{r1} \left(\frac{\varepsilon_0}{\varepsilon_r}\right)_i e^{-\left(\frac{\rho_i}{(n_i+n_{eq}(b_j))}\right)^{\beta_i}} \overline{\varepsilon_{v1}}(b_j) \left(\frac{1-e^{-Q_i(b_j)h_{bedrock}}}{Q_i(b_j)}\right) I_{r(b_j)\leq 1} + \widetilde{\delta(x)}^{i-1} I_{r(b_j)>1} \right] R_k(b_j)$$

Approximated rutting profile

$$\vec{H}_0^i = \frac{\vec{H}_0^i}{2} \text{ (Equation 35)}$$

$$\widetilde{\delta(x)}^i = \sum_{k=0}^{p} \vec{H}_k^i R_k(x)$$

Figure 46. Equation. Algorithm 2: The algorithm for simulating the rutting-profile accumulation using Chebyshev polynomials.

Algorithm 3: The algorithm for simulating rutting profile accumulation using Chebyshev Polynomials

$\vec{H}_k^1 = 0$ (Initialization) **for** $i = 1$ *to* M *(Total Number of Steps)* **do**

$$\vec{H}_k^i = \vec{H}_k^i + \frac{2}{p+1} \sum_{j=0}^{p} DI(b_j) R_k(b_j) \text{ for } k \geq 0$$

$$\vec{H}_0^M = \frac{\vec{H}_0^M}{2}$$

$$\widetilde{DI(x)}^M = \sum_{k=0}^{p} \vec{H}_k^M R_k(x)$$

Figure 47. Equation. Algorithm 3: The algorithm for simulating the damage-index profile accumulation using Chebyshev polynomials.

CHAPTER 5: NUMERICAL EXAMPLE

In this section, an example demonstrates the framework developed. Due to the brevity of this paper, which focuses on the concept and equations behind the framework, we preferred to present a simple but illustrative example. The pavement section considered in the example is shown in Figure 48. Following algorithm 1, this pavement section was divided into 15 sub-layers. The loadings considered in the example are two identical dual-tire assemblies (DTA) that are shifted to the left by 16 in. and 8 in. from the center of the road. DTA has an axle load of 18 kips, with 125 psi of tire pressure. The standard deviation for wheel wander is assumed to be 1 in., which can be interpreted as channelized traffic such as ACTs (recommended value for human-driven trucks is 10 in.). The number of repetitions for the loads is assumed to be 1,000 (i.e., n = 1,000). The degree of Chebyshev approximation is selected as 50. Assumed typical values for all the constants used in the transfer functions are presented in Table 2.

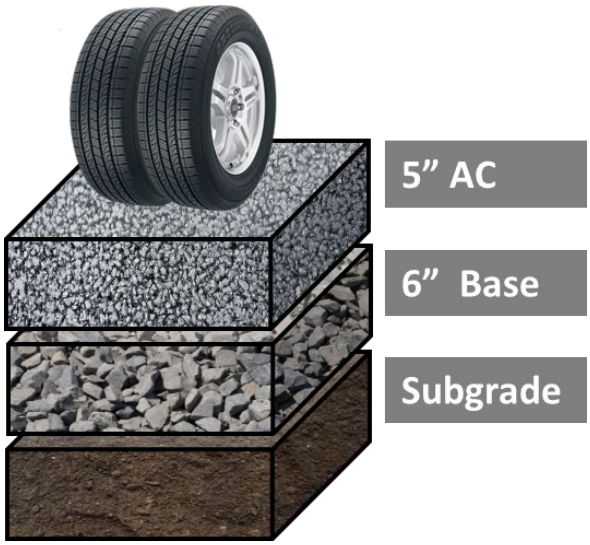

Figure 48. Photo. The pavement section considered in the example.

Table 2. Assumed Values for the Constants Used in Empirical Functions

Variable Name	Value	Variable Name	Value
Initial IRI	60 in./mi	Percent plasticity index of the soil	4
AC temperature	72 F	Age	0.1 year
Lane width	12 ft	Resilient modulus of base	40000 psi
Axle width	8 ft	Resilient modulus of subgrade	5000 psi
Average annual precipitation	39.2 in.	Groundwater table depth	10 ft
Freezing Index	50	Effective asphalt content by volume	4.6
Percent passing the 0.02-mm sieve	2	Percent air voids	4
Percent passing the 0.075-mm sieve	7		

Figure 49 shows the rutting profile computed after the first load application at each sub-layer. It should be noted that the first three sub-layers were omitted because there was no compressive strain within these layers. Therefore, the results were presented for 12 sub-layers. In the figures, the x-axis stands for the wheel path, which changes -3 ft to 3 ft (half-lane width); and the y-axis shows the damage profiles. Because the assumed standard deviation is very small (i.e., 1 in.), the shape of DTA loading is reflected in the computed rutting profiles, which can be observed in Figure 49-A, 49-B, 49-C, and 49-D. However, the shape of DTA loading starts to disappear as the depth of the response increases. For example, rutting profiles for all sub-layers within the subgrade (Figure 49-E to 49-L) exhibit the profiles with only one peak. Moreover, the rutting profile gets wider as the depth increases, which matches field observations: Subgrade rutting manifests itself as much wider rutting at the pavement surface, as compared to AC rutting. Figure 50 presents the damage index for fatigue-cracking computation, both top-down and bottom-up cracking. As can be seen, fatigue cracking also is not affected by the shape of loading.

Figure 51 presents the accumulated damage after the second load application. The highest impact of shifting was observed within the sub-layers that are close to the surface (Figure 51-A to 51-D). However, as the depth increases, the impact of shifting also decreases, which matches the findings in the literature. The rutting profile becomes wider under wheel wander for deeper sub-layers. Figure 51 shows damage-index profiles after the second step. After summing all the rutting profiles given in Figure 52 and plugging the total into Figure 32, along with fatigue cracking, the IRI profile can be computed as given in Figure 52-C. It should be noted that this roughness profile was obtained after only two load applications. The IRI profile exhibits a more irregular behavior when many more loadings with different lateral positions are applied.

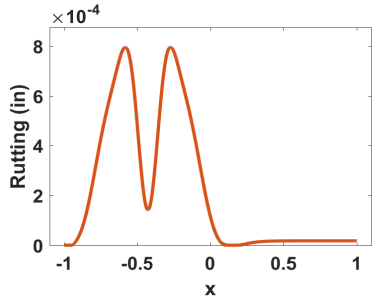

(a) Sub-layer 1 (AC)

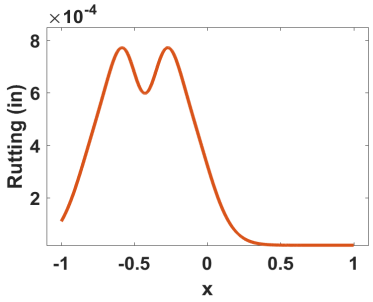

(b) Sub-layer 2 (AC)

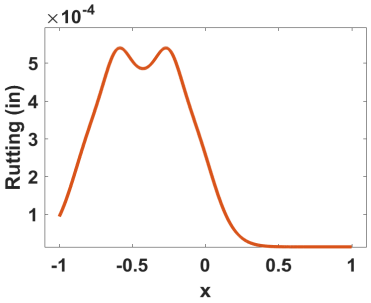

(c) Sub-layer 3 (AC)

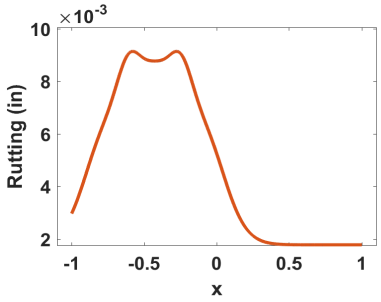

(d) Sub-layer 4 (Base)

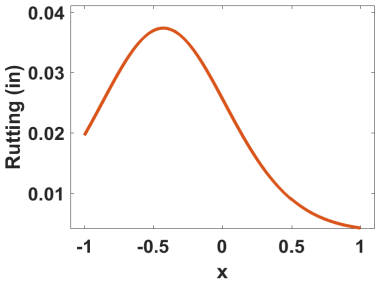

(e) Sub-layer 5 (Base)

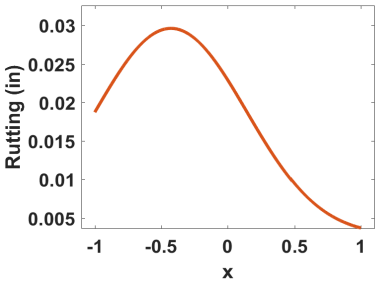

(f) Sub-layer 6 (Subgrade)

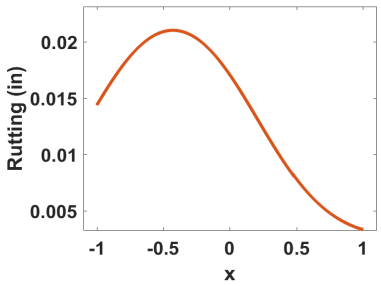

(g) Sub-layer 7 (Subgrade)

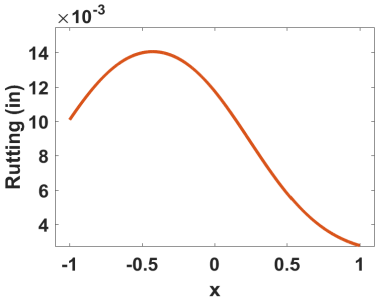

(h) Sub-layer 8 (Subgrade)

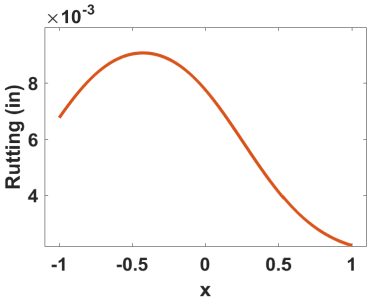

(i) Sub-layer 9 (Sub-grade)

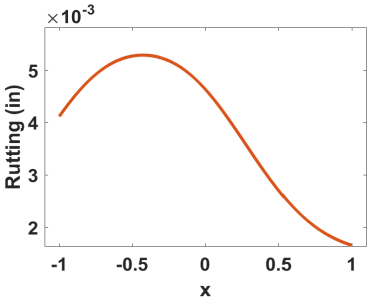

(j) Sub-layer 10 (Subgrade)

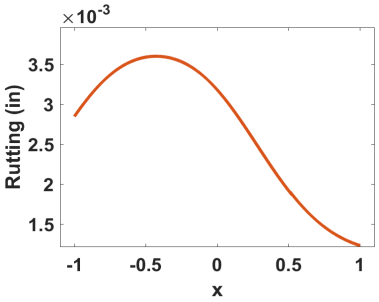

(k) Sub-layer 11 (Subgrade)

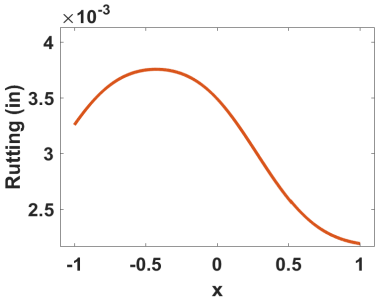

(i) Sub-layer 12 (After 8 ft)

Figure 49. Graph. Accumulated rutting profiles after the first load application.

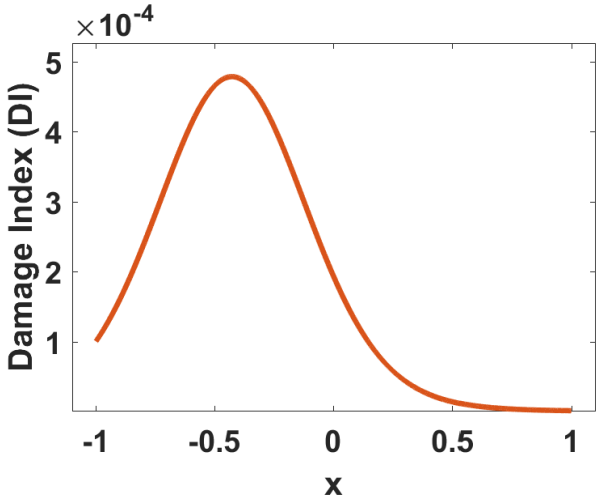

(a) Top-down cracking

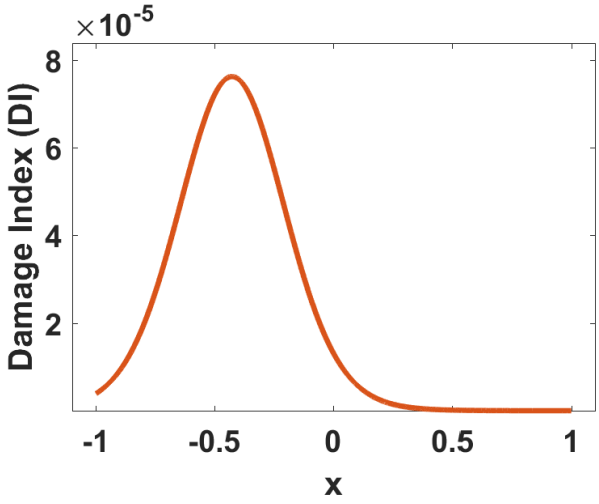

(b) Bottom-up cracking

Figure 50. Graph. Damage-index (Figure 8) profiles after the first load application.

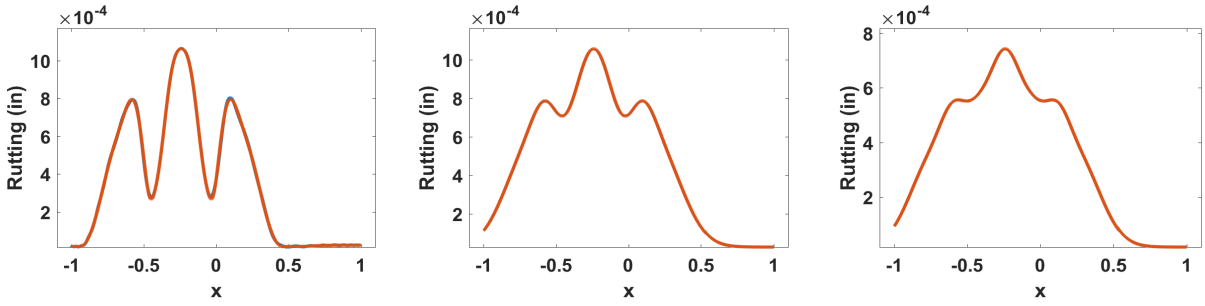

(a) Sub-layer 1 (AC) (b) Sub-layer 2 (AC) (c) Sub-layer 3 (AC)

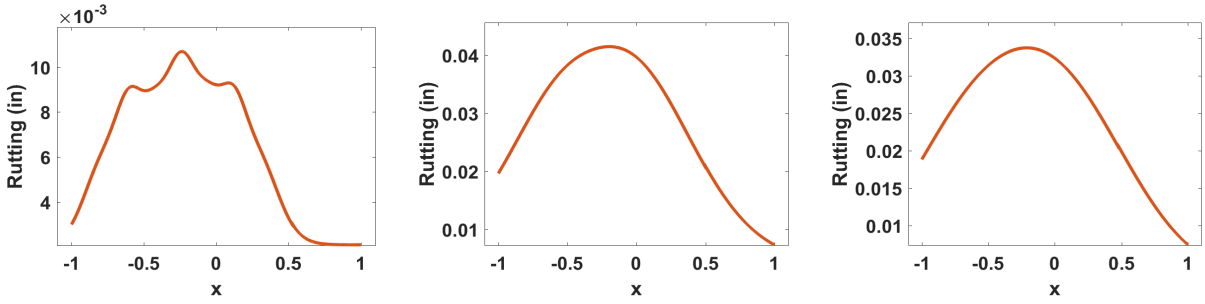

(d) Sub-layer 4 (Base) (e) Sub-layer 5 (Base) (f) Sub-layer 6 (Subgrade)

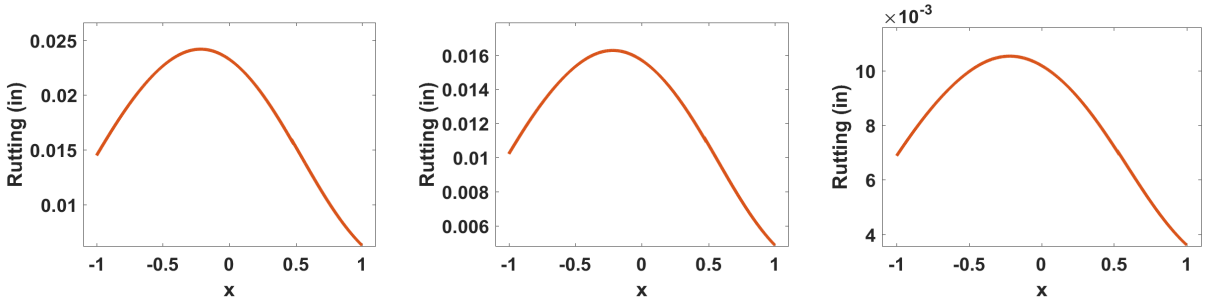

(g) Sub-layer 7 (Subgrade) (h) Sub-layer 8 (Subgrade) (i) Sub-layer 9 (Subgrade)

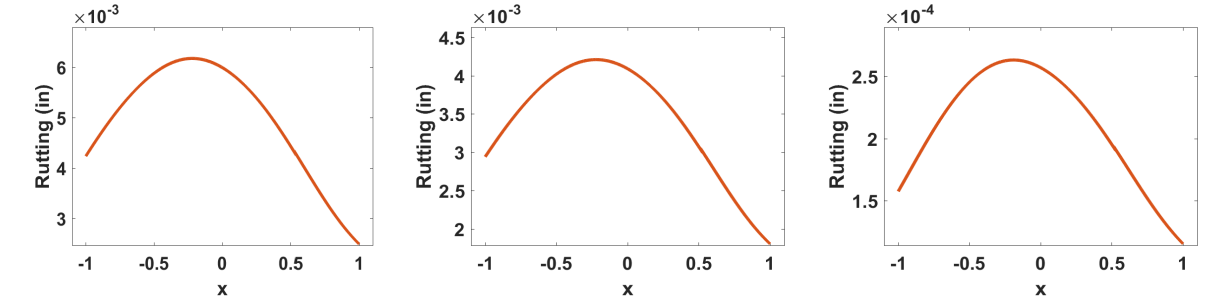

(j) Sub-layer 10 (Subgrade) (k) Sub-layer 11 (Subgrade) (i) Sub-layer 12 (After 8 ft)

Figure 51. Graph. Accumulated rutting profiles after the second load application.

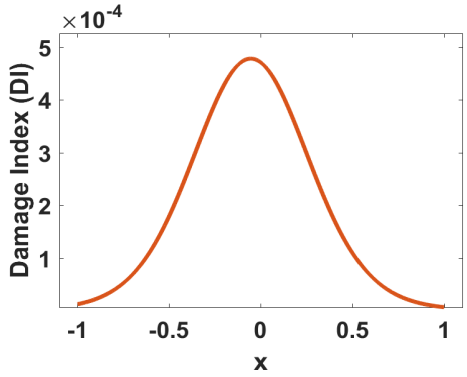

(a) Top-down cracking

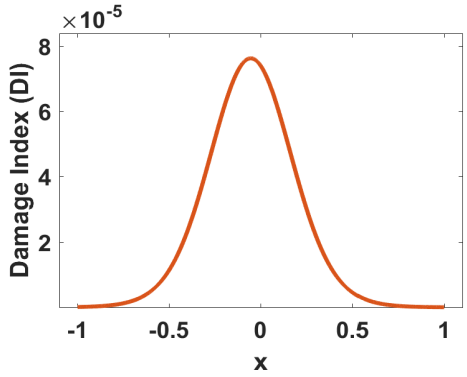

(b) Bottom-up cracking

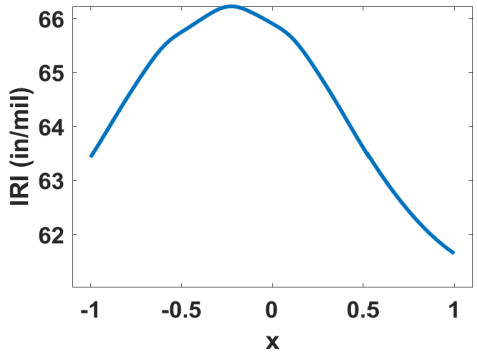

(c) IRI

Figure 52. Graph. Damage index and IRI profiles after the second load application.

CHAPTER 6: DISCUSSION

Results of the example demonstrated the capability of the framework developed, as the damage accumulation within pavement was simulated by explicitly considering the lateral position of wheel loading, lane width, and axle width. It should be noted that although MEPDG's damage approach was used in this paper, the concept behind Wander 2D can be applied on any pavement-design approach as long as the damage can be computed at discrete points along the pavement cross section. Further observations and discussion about the framework are presented in two groups in the remainder of this section.

INCREASING DIMENSIONALITY OF PAVEMENT DESIGN

The state-of-the-practice pavement-design guideline, MEPDG, reports a single number as a decision criteria because, as explained in Chapter 2, MEPDG averages the damage over the cross section. On the contrary, the framework developed outputs a continuous damage profile. In other words, this framework increases the dimensionality of pavement design from one dimension (depth only) to two dimensions (depth and transverse direction). This creates two challenges.

The first challenge is that failure criteria may need to be revisited because the existing criteria are defined solely based on the magnitude of the distresses, whereas lateral characteristics of damage distresses (e.g., width) also become a decision factor with the framework developed. The second challenge is that new calibration techniques (rather than an average) may be required to calibrate the transfer functions for the transverse profile.

LIMITATIONS FOR MEPDG'S DAMAGE-ACCUMULATION APPROACH

There are two main limitations of emprical functions used in MEPDG for consideration of ACTs. The first and most important one is that resting period, which is one of the most significant variables affecting the behavior of asphalt concrete, is not explicitly taken into account. Especially with the introduction of platooning, the characteristics of the resting period observed in the field are expected to change drastically. Therefore, explicit consideration of the resting period becomes necessary for accurate assessment of the impact of ACTs. The second is the transfer function used for simulating rutting in granular materials. If previously accumulated rutting is too small and if the response applied at the current step is not large enough, the time-hardening approach fails due to the structure of the transfer function. In this study, this limitation is overcome numerically by employing identity functions given in algorithm 2. However, more robust empirical functions are needed for granular materials.

CHAPTER 7: SUMMARY AND CONCLUSION

Introduction of autonomous and connected trucks (ACTs) is expected to improve highway freight operations. ACTs are expected to increase fuel efficiency and productivity while decreasing congestion and operation costs. However, their introduction may require changes and modifications to existing transportation-infrastructure design and management guidelines because the characteristics of the inputs to such guidelines may drastically change due to introduction of ACTs.

This paper analyzed one such input to pavement design: the lateral position of loading. The lateral position of loading is a random phenomenon for human-driven trucks, as they do not follow a straight path when they travel. Therefore, this variable has been considered in an implicit way in existing pavement-design guidelines (i.e., wheel wander). However, due to enabling technologies embedded in ACTs, this variable will be much less random and, more importantly, controllable. Therefore, it needs to be considered explicitly (i.e., as a direct input in pavement design) rather than implicitly.

This study presented a framework that can improve any pavement damage-accumulation approach (i.e., pavement design) to take the lateral position of loading as an explicit input. Due to using truncated normal distributions, the effects of lane width and vehicle width on pavement-damage accumulation could be considered in the framework as well. In this paper, this framework was applied to the state-of-the-practice pavement-design approach MEPDG. MEPDG's damage-accumulation equations were reinforced with curve-fitting and function-approximation techniques for explicit consideration of the lateral position. A simple numerical example was presented to demonstrate how accumulated damage varies with respect to the position of loading.

Future work includes improving the curve-fitting part of the framework to make it fully autonomous because it still requires a user-defined parameter. Additionally, we plan to increase the dimensionality to 3D by fitting the 2D curve to computed damages at discrete locations (i.e., in both lateral and longitudinal directions). Finally, the resting period, another important input for pavement design whose characteristics are expected to be affected by the introduction of ACTs, will be incorporated into the framework.

REFERENCES

AASHTO. (2015). *Mechanistic-empirical pavement design guide: A manual of practice*. AASHTO.

Al-Qadi, I. L., J. A. Hernandez, A. Gamez, M. Ziyadi, O. E. Gungor, & S. Kang. (2015). Impact of wide-base tires on pavements: A national study. *Transportation Research Record: Journal of the Transportation Research Board* 0361198118757969.

Al-Qadi, I. L., & H. Wang. (2012). Impact of wide-base tires on pavements: Results from instrumentation measurements and modeling analysis. *Transportation Research Record: Journal of the Transportation Research Board (2304)*: 169–76.

American Society of Civil Engineering (ASCE). (2017). *2017 infrastructure report card*. ASCE.

American Trucking Associations (ATA). (2017). *Truck driver shortage analysis*. ATA.

Castillo, D., & I. Al-Qadi. (2018). Importance of heterogeneity in asphalt pavement modeling. *Journal of Engineering Mechanics 144*(8): 04018060.

Elseifi, M. A., I. L. Al-Qadi, & P. J. Yoo. (2006). Viscoelastic modeling and field validation of flexible pavements. *Journal of Engineering Mechanics 132*(2): 172–78.

Gungor, O. E., I. L. Al-Qadi, A. Gamez, & J. A Hernandez. (2016). In-situ validation of three-dimensional pavement finite element models. In *The Roles of Accelerated Pavement Testing in Pavement Sustainability*, 145–59. Springer.

Gungor, O. E., I. L. Al-Qadi, A. Gamez, & J. A. Hernandez. (2017). Development of adjustment factors for MEPDG pavement responses utilizing finite-element analysis. *Journal of Transportation Engineering, Part A: Systems 143*(7): 04017022.

Gungor, O. E., J. A. Hernandez, A. Gamez, & I. L. Al-Qadi. (2016). Quantitative assessment of the effect of wide-base tires on pavement response by finite element analysis. *Transportation Research Record: Journal of the Transportation Research Board (2590)*: 37–43.

Hernandez, J., & I. L. Al-Qadi. (2016). Semicoupled modeling of interaction between deformable tires and pavements. *Journal of Transportation Engineering—Part A: Systems 143*(4): 04016015.

Islam, M. R., R. A. Tarefder, & I. Syed. (2014). Measurements of lateral distribution of vehicle wheels and its effect on fatigue life of asphalt concrete. *Sustainability, Eco-efficiency, and Conservation in Transportation Infrastructure Asset Management* 379.

Luo, W., & K. C. P. Wang. (2013). Wheel path wandering based on field data. In *Airfield and Highway Pavement 2013: Sustainable and Efficient Pavements*, 506–15.

National Cooperative Highway Research Program (NCHRP). (2004). *Guide for mechanistic-emprical design of new and rehabilitated pavement structures*.

Noorvand, H., G. Karnati, & B. S. Underwood. (2017). Autonomous vehicles: Assessment of the implications of truck positioning on flexible pavement performance and design. *Transportation Research Record: Journal of the Transportation Research* Board (2640): 21–28.

Pierce, D., & D. Murray. (2014). *Cost of congestion to the trucking industry*.

Royal Automobile Club Foundation for Motoring (RAC) (2017). *Readiness of the road network for connected and autonomous vehicles.*

Siddharthan, R. V., M. Nasimifar, X. Tan, & E. Y. Hajj. (2017). Investigation of impact of wheel wander on pavement performance. *Road Materials and Pavement Design 18*(2): 390–407.

U.S. Department of Transportation Bureau of Transportation Statistics. (2015). *Freight facts and figures*.

Wang, H., & I. L. Al-Qadi. (2010). Impact quantification of wide-base tire loading on secondary road flexible pavements. *Journal of Transportation Engineering 137*(9): 630–39.

Wu, R., & J. T. Harvey. (2008). Evaluation of the effect of wander on rutting performance in HVS tests. In *Proceedings of the 3rd International Conference on Accelerated Pavement Testing.*

Yoo, P. J., & I. L. Al-Qadi. (2007). Effect of transient dynamic loading on flexible pavements. *Transportation Research Record 1990*(1): 129–40.